

Quantum Spin-Valley Hall Kink States: From Concept to Materials Design

Tong Zhou^{1,*} Shuguang Cheng^{1,2} Michael Schleienvoigt,³ Peter Schüffelgen,³ Hua Jiang^{1,4}, Zhongqin Yang,⁵ and Igor Žutić^{1,†}

¹Department of Physics, University at Buffalo, State University of New York, Buffalo, New York 14260, USA

²Department of Physics, Northwest University, Xi'an 710069, China

³Peter Grünberg Institute 9, Forschungszentrum Jülich & JARA Jülich-Aachen Research Alliance, 52425 Jülich, Germany

⁴School of Physical Science and Technology, Soochow University, Suzhou 215006, China

⁵State Key Laboratory of Surface Physics and Key Laboratory of Computational Physical Sciences (MOE) and Department of Physics and Collaborative Innovation Center of Advanced Microstructures, Fudan University, Shanghai 200433, China

(Received 25 October 2020; revised 13 May 2021; accepted 12 August 2021; published 9 September 2021)

We propose a general and tunable platform to realize high-density arrays of quantum spin-valley Hall kink (QSVHK) states with spin-valley-momentum locking based on a two-dimensional hexagonal topological insulator. Through the analysis of Berry curvature and topological charge, the QSVHK states are found to be topologically protected by the valley-inversion and time-reversal symmetries. Remarkably, the conductance of QSVHK states remains quantized against both nonmagnetic short- and long-range and magnetic long-range disorder, verified by the Green-function calculations. Based on first-principles results and our fabricated samples, we show that QSVHK states, protected with a gap up to 287 meV, can be realized in bismuthene by alloy engineering, surface functionalization, or electric field, supporting nonvolatile applications of spin-valley filters, valves, and waveguides even at room temperature.

DOI: 10.1103/PhysRevLett.127.116402

Two-dimensional (2D) hexagonal lattices offer a versatile platform to manipulate charge, spin, and valley degrees of freedom and implement different topological states. While pioneering predictions for the quantum anomalous and quantum spin Hall (QSH) effects [1,2] were guided by graphenelike systems, graphene poses inherent difficulties with its weak spin-orbit coupling (SOC) and a gap of only $\Delta \sim 40 \text{ } \mu\text{eV}$ [3]. The quest for different 2D hexagonal monolayers (MLs) with a stronger SOC on one hand reveals, as in transition metal dichalcogenides, an improved control of valley-dependent phenomena [4], emulating extensive research in spintronics [5], while on the other hand, as in a ML Bi on SiC (Bi/SiC) substrate, topological states remain even above room temperature with a huge topological gap $\sim 0.8 \text{ eV}$ [6]. However, examples where valley degrees of freedom support robust topological states are scarce.

In 2D materials with broken inversion symmetry, such as gapped graphene [7–12] and transition metal dichalcogenides [13,14], the opposite sign of the momentum-space Berry curvature $\Omega(\mathbf{k})$ in different valleys is responsible for a valley Hall effect, where the carriers in different valleys turn into opposite directions transverse to an in-plane electric field [7,14]. A striking example of such a sign reversal in $\Omega(\mathbf{k})$ [see also Fig. 1] along an internal boundary of a film is realized in quantum valley Hall kink (QVHK) states [15–29]. The resulting topological defect supports counterpropagating 1D chiral electrons, topologically protected by the valley-inversion symmetry [15–19].

The underlying mechanism for the formation of zero-energy states, expected from the index theorem [30,31], shares similarities with many other systems in condensed matter and particle physics [32–39]. While the proposals for QVHK mainly focus on bilayer graphene (BLG) systems [20–24], the required sign reversal in $\Omega(\mathbf{k})$ realized by either the random local stacking faults [20,22] or a dual-split-gate structure [21,23,24] is challenging to implement to achieve high-density channels. With the required applied electric field, the volatility of

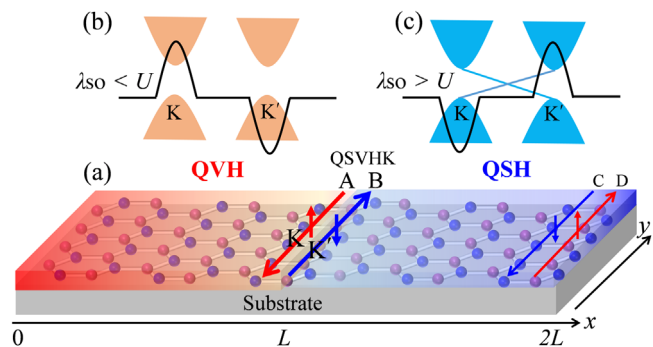


FIG. 1. (a) Schematic of the QSVHK states (*A, B*) at the valleys *K* and *K'*, and QSH edge states (*C, D*) in a junction formed by QVH and QSH insulators. $2L$ is the junction length. The red (blue) arrow denotes the spin-up (down) channel. (b),(c) The schematic of the bands and Berry curvatures (black lines) for QVH and QSH insulators, distinguished by the relative strength of the SOC, λ_{SO} , and staggered potential U .

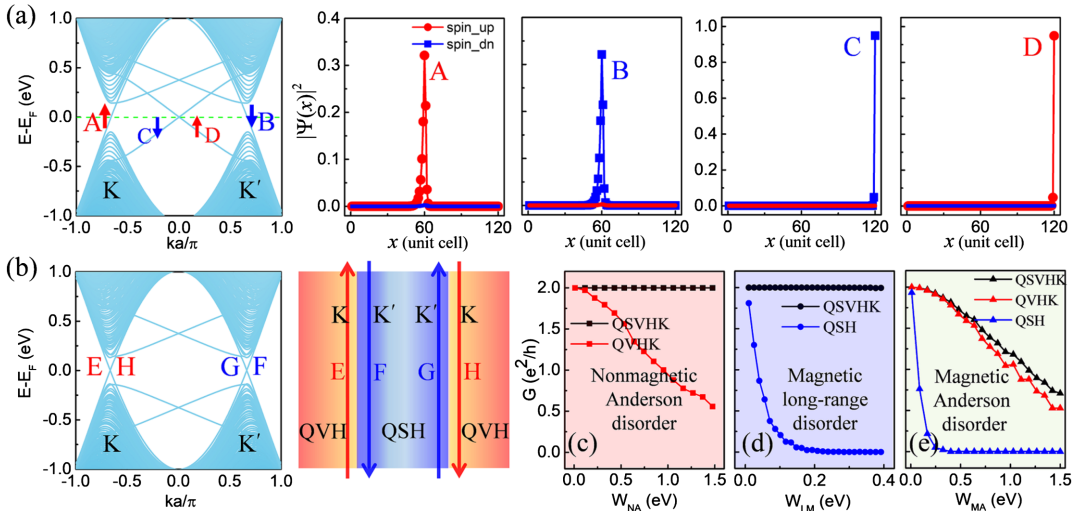


FIG. 2. (a) Bands and wave function distributions ($|\Psi(x)|^2$) for topological states $A-D$ in the QSH-QVH junction with $L = 60$ unit cells. (b) Bands and schematic of the QVH-QSH-QVH junction with pure QSVHK states $E-H$. (c) Junction conductance G versus nonmagnetic Anderson disorder strength W_{NA} at the Fermi level for the QSVHK and QVHK states. (d) Same as (c) but for the QSVHK and QSH states versus magnetic long-range disorder strength W_{LM} . (e) Same as (c) but versus magnetic Anderson disorder strength W_{MA} . The parameters U, λ_{SO} for the QVH and QSH regions are taken from the BiAs on SiC (BiAs/SiC) and Bi/SiC, respectively. The hopping parameter is $t_{1,2} = 1$ eV.

QVHK limits their envisioned use in valleytronics. A small gap of $BLG \sim 20$ meV [21] excludes high-temperature applications, and QVHK states were limited to 5 K [20–24]. Crucially, disorder easily induces intervalley scattering, preventing the expected ballistic transport in QVHK states [20,21,29].

Motivated by these challenges, we propose a robust platform to realize high-density arrays of spin-polarized QVHK states at room temperature based on a 2D hexagonal topological insulator, where the QVHK states are simultaneously the QSH edge states, forming along the QSH-quantum valley Hall (QVH) interface as shown in Fig. 1. The QSH is described by a topological invariant $Z_2 = 1$ [2], while the QVH is characterized by a quantized valley Chern number $C_V = 1$ and $Z_2 = 0$ [8,19]. Across their interface, both Z_2 and C_V change the value; thus the QSH and QVHK states simultaneously emerge along the interface, giving largely unexplored topological kink states that we term quantum spin-valley Hall kink (QSVHK) states. Unlike the previous studies of the interplay between topological states [15–29,36–46], our proposed QSVHK state shows a peculiar marriage between the QSH and QVH. The QSH becomes robust against the magnetic long-range disorder due to the valley-inversion symmetry protection of the QVH [15–19], while the QVH can be robust against the nonmagnetic short-range disorder because of the time-reversal symmetry protection of the QSH [2,47]. Thus, in contrast to the trivial spin-valley Hall effects [48–50], the topological QSVHK states are robust against both nonmagnetic short- and long-range and magnetic long-range disorder, giving robust ballistic spin-valley-momentum locking transport. The QSH-QVH

junction can be implemented by inducing a staggered potential, U , in a part of the 2D topological insulators. When U is smaller (larger) than the strength of the intrinsic SOC, λ_{SO} , the QSH (QVH) state is obtained. Our first-principles calculations reveal that U can be induced by alloy engineering or surface decoration and easily controlled by the electric field.

We first present our idea through the analysis of a tight-binding model based on p_x and p_y orbitals, which is widely used to describe the physics of the hexagonal MLs, including arsenene [51,52], antimonene [41,42,53,54], bismuthene [6,50,55], and binary element group-V MLs [56,57]:

$$H = \lambda_{SO} \sum_i c_i^\dagger \sigma_z \otimes s_z c_i + \sum_i U_i c_i^\dagger \sigma_0 \otimes s_0 c_i + \left(\sum_i \sum_{j=1,2,3} c_i^\dagger T_{\delta_j} c_{i+\delta_j} + \text{H.c.} \right). \quad (1)$$

Here, c_i represents the annihilation operator on site i . σ and s indicate the Pauli matrices acting on orbital and spin spaces. The first term describes the intrinsic SOC, and the second term gives the staggered potential with $U_i = U(-U)$ for the $A(B)$ sublattice. The hopping term

$$T_{\delta_j} = \begin{bmatrix} t_1 & z^{(3-j)} t_2 \\ z^j t_2 & t_1 \end{bmatrix} \otimes s_0 \quad (2)$$

describes the nearest hopping from site i to $i + \delta_j$, where $z = \exp(2i\pi/3)$ and $t_{1/2}$ is the hopping coefficient. In the absence of the first two terms in Eq. (1), the gapless Dirac

points exist at the two valleys [50,55]. The staggered potential and intrinsic SOC open a gap of $2|\lambda_{SO} - U|$ at the Dirac points and their competition determines the topology of the system. When $\lambda_{SO} < U$, the system is in QVH with $Z_2 = 0$ and opposite $\Omega(\mathbf{k}) \neq 0$ at the two valleys [Fig. 1(b)]. When $\lambda_{SO} > U$, the system is in QSH with $Z_2 = 1$ and for $U > 0$ the $\text{sgn}[\Omega(\mathbf{k})]$ is reversed as compared to the QVH [Fig. 1(c)]. We consider a planar junction formed by the QVH and QSH [Fig. 1(a)], where the QSVHK state emerges along their interface, since both Z_2 and $\Omega(\mathbf{k})$ change the sign.

To identify such QSVHK states, we calculate the spectrum of the QSH-QVH junction along the zigzag direction, where the valley degree can be preserved [29,58,59]. As shown in Fig. 2(a), there are four non-degenerate gapless states, $A-D$, in the bulk band gap. The helical C and D states are the common QSH states localized at the outer edge of the QSH region, verified by their wave functions in Fig. 2(a). The A (B) state at the K (K') valley shows the QSVHK state localized at the inner interface [Fig. 2(a)]. Unlike the QVHK state in BLG, the QSVHK state is fully spin-polarized. Specifically, the kink state A (B) at K (K') valley has a spin-up (down) channel. Such spin-valley-momentum locking supports a perfect spin-valley filter.

To better understand the emergence of the QSVHK state, we focus on the low-energy physics of Eq. (1). We expand the Hamiltonian around the valleys and obtain a continuum model:

$$H = \hbar v_F(k_x \sigma_x + \tau_z k_y \sigma_y) + \lambda_{SO} s_z \tau_z \sigma_z + U \sigma_z, \quad (3)$$

where v_F is the Fermi velocity, σ , s , and τ are the Pauli matrix for orbital, spin, and valley, respectively. From the index theorem [30], the number of the kink channels is related to the change of the bulk topological charges across the interface [15,19,60]. The spin- and valley-projected topological charge $C_{\tau_z}^{s_z}$ can be calculated by integrating the spin-dependent $\Omega(\mathbf{k})$ of the valence bands around each valley [15,19,60]. From the continuum model in Eq. (3), we obtain

$$C_{\tau_z}^{s_z} = \frac{\tau_z}{2} \text{sgn}(U - \tau_z s_z \lambda_{SO}). \quad (4)$$

In the QVH region, we get $(C_K^\uparrow, C_K^\downarrow, C_{K'}^\uparrow, C_{K'}^\downarrow) = (0.5, 0.5, -0.5, -0.5)$ and in the QSH region $(C_K^\uparrow, C_K^\downarrow, C_{K'}^\uparrow, C_{K'}^\downarrow) = (-0.5, 0.5, -0.5, 0.5)$. The number of the kink modes per spin or valley $(\nu_K^\uparrow, \nu_K^\downarrow, \nu_{K'}^\uparrow, \nu_{K'}^\downarrow)$ is an integer evaluated from the difference between the topological charges in two regions [15,19], i.e., $(\nu_K^\uparrow, \nu_K^\downarrow, \nu_{K'}^\uparrow, \nu_{K'}^\downarrow) = (1, 0, 0, -1)$. It is clear the spin-up (down) topological charge has an integer change at the K (K') valley, giving the spin-valley polarized QSVHK state. This topological charge analysis is consistent with

our discussion about the energy spectrum in Fig. 2(a). In QSH-QVH junctions, there are still QSH states along the outer edge. To eliminate them and realize a pure QSVHK transport, we propose in Fig. 2(b) a QVH-QSH-QVH junction, where the two pairs of QSVHK states are verified by the calculated bands. Multiple channels can be expected with more QSH-QVH boundaries, where the width of each region should be large enough to avoid the interplay between adjacent QSVHK states.

For valley-related transport, the influence of the short-(long)-range disorder is usually significantly different since the former (latter) induces (excludes) intervalley scattering [61]. The former (latter) is characterized by the smaller (larger) disorder correlation length λ compared to the lattice spacing a [61]. For example, the QVHK state is only robust against the long-range disorder [15–24]. To explore the robustness of the QSVHK state against the disorder, we calculate the junction conductance G using the Landauer-Büttiker formula [62] and the Green-function method [63–66] in the presence of nonmagnetic Anderson disorder ($\lambda \rightarrow 0$) [64,67] in the energy range $(-W_{NA}/2, W_{NA}/2)$, magnetic Anderson disorder [65,68] $(-W_{MA}/2, W_{MA}/2)$, and magnetic long-range ($\lambda = 7a$) disorder [69,70] $(-W_{LM}/2, W_{LM}/2)$, where W_{NA} , W_{MA} , and W_{LM} measure their respective strengths. For comparison, we calculate $G(W_{NA})$, $G(W_{LM})$, and $G(W_{MA})$ in QVHK and QSH states, shown in Figs. 2(c)–(e). See calculation details and the crossover between the short- and long-range disorder in the Supplemental Material [71]. For the QVHK state with valley-momentum locking, its G decreases with W_{NA} increases, consistent with previous studies [20,21], because the Anderson disorder breaks the valley-inversion symmetry and leads to the intervalley scattering. For the QSH state with spin-momentum locking, its G decreases with W_{LM} (W_{MA}), because the time-reversal symmetry is broken by the magnetic disorder, in agreement with the experiments [80,81]. In contrast, for the QSVHK state with spin-valley-momentum locking protected by both valley-inversion and time-reversal symmetries, its G remains quantized against both nonmagnetic Anderson disorder and magnetic long-range disorder [Figs. 2(c),(d)]. The backscattering in the QSVHK state can only be induced by simultaneously breaking the valley-inversion and time-reversal symmetries—for example, by magnetic Anderson disorder [Fig. 2(e)]. However, with W_{MA} , the G of the QSVHK state is still higher than that of the QSH and QVHK states, since simultaneously scattering spin and valley is harder than scattering each of them.

Material design.—The key factor to achieve QSVHK is creating an interface of the QSH and QVH. Since there are a large number of hexagonal QSH insulators [58], a natural way to obtain such an interface is to engineer a part of QSH insulator into a QVH region, where $U > \lambda_{SO}$ is required. Recently, group-V MLs bismuthene, antimonene, and arsenene on a SiC substrate were predicted to be

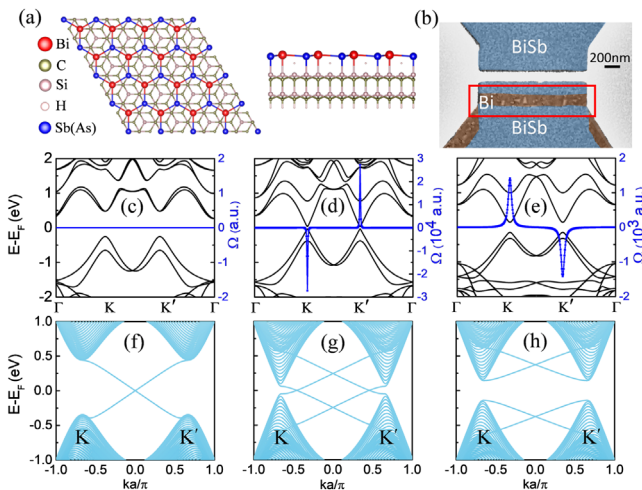


FIG. 3. (a) Top and side views of a ML BiSb or BiAs on a SiC substrate. (b) Scanning electron micrograph image of the planar BiSb-Bi-BiSb junction with a Si_3N_4 stencil mask (gray) 300 nm above the film for shadowing. BiSb-Bi interfaces are marked by the red rectangle. (c)–(e) Bands (black) and Berry curvatures, $\Omega(\mathbf{k})$ (blue), of the valence bands for the Bi/SiC, BiSb/SiC, and BiAs/SiC, respectively. (f)–(h) Bands of the zigzag nanoribbons for the Bi/SiC, BiSb/SiC, and BiAs/SiC, respectively. The fitted parameters (λ_{SO} , U) for Bi/SiC, BiSb/SiC, and BiAs/SiC are (0.44 eV, 0 eV), (0.30 eV, 0.26 eV), and (0.24 eV, 0.38 eV), respectively.

high-temperature 2D topological insulators [82]. For Bi/SiC, a huge nontrivial gap of 0.8 eV has been measured [6], originating from the intrinsic SOC of Bi $p_{x,y}$ orbitals [71]. However, with its inversion symmetry, Bi/SiC fails to show valley-dependent effects, as verified by $\Omega(\mathbf{k}) = \mathbf{0}$ at all \mathbf{k} [Fig. 3(c)]. To break the inversion symmetry, we propose to use alloy engineering to induce U in bismuthene, a well-established approach to tailor electronic and topological properties [83,84]. Specifically, we propose to grow binary group-V MLs BiSb or BiAs on the SiC substrate, depicted in Fig. 3(a). We expect the change in the binary composition alters the strength of SOC (growing with the atomic number Z) and U (growing with a relative difference in Z of the two group-V elements), thus favoring either QVH or QSH insulators, as shown in Fig. 1(a). BiSb and BiAs films can be fabricated using molecular beam epitaxy [Fig. 3(b)] similar to that growth of Bi/SiC or exfoliated from bulk [51,52]. From first-principles calculations, we see the BiSb/SiC and BiAs/SiC bands near E_F can be accurately described by the Hamiltonian in Eq. (1) [71].

Without considering SOC, Bi/SiC has gapless Dirac bands at two valleys, while the trivial gaps of 0.52 eV and 0.76 eV are opened in BiSb/SiC and BiAs/SiC [71], respectively. Such gaps, originating from the staggered potential, give $U_{\text{BiSb/SiC}} = 0.26$ eV and $U_{\text{BiAs/SiC}} = 0.38$ eV. With SOC, a nontrivial gap of 66 meV is opened in BiSb/SiC with $\Omega(\mathbf{k}) \neq \mathbf{0}$ [Fig. 3(d)], giving a QSH

insulator with $Z_2 = 1$ and the helical edge states [Fig. 3(g)]. The edge states outside the gap are not useful for the robust dissipationless transport because they are negligible compared to the huge contribution from the trivial bulk bands [47]. Figure 3(e) reveals a different situation for BiAs/SiC. Because of $U > \lambda_{\text{SO}}$, a gap of 287 meV appears at K and K' with $Z_2 = 0$ and no topological edge states [Fig. 3(h)]. Compared to BiSb/SiC, the sign reversal of $\Omega(\mathbf{k})$ for BiAs/SiC gives the desired QVH phase.

The resulting QSH-QVH junction [Fig. 1] can be realized combining BiAs/SiC (QVH) with Bi/SiC (QSH) or BiSb/SiC (QSH). Alternatively, to simplify the fabrication and yield QSH with an even larger nontrivial gap, the BiAs-Bi/SiC junction is desirable where the verified QSVHK states are shown in Fig. 2(a). In this analysis, we exclude Rashba SOC [5] since its influence is negligible in QSVHK as discussed in the Supplemental Material [71]. The BiAs-Bi/SiC junction provides a robust platform for QSVHK, protected by a global gap of 287 meV, which is ~ 14 times larger than in BLG [21], supporting ballistic transport at high temperatures, verified by the finite-temperature Green-function calculations and discussion about the influence of the many-body interaction [71].

The desired QSH-QVH junction can be fabricated using our well-established molecular beam epitaxy selective area growth and stencil lithography [85] as shown in Fig. 3(b). The fabrication process and the influence of the stoichiometry are demonstrated in [71]. Multiple QSH-QVH boundaries can be created by spatially selective deposition [85,86], enabling transport of high-density channels. A QSVHK state robust against nonmagnetic and long-range disorder and insensitive to the interface configurations [71] facilitates its experimental observation and possible applications. Unlike the QVHK state in BLG, the QSVHK state in bismuthene is spin-polarized and requires no external field. This offers nonvolatility in unexplored applications coupling spin and valley, going beyond low-temperature BLG valleytronic applications [23]. For example, the QSVHK state supports fully spin-polarized quantum valley currents, making spin-valley filters, valves, and waveguides possible, or extends the functionalities for spin interconnects [87–89].

Another way to realize the QSVHK state in a bismuthene system is surface decoration, widely used to modify the properties of the 2D materials [90]. Particularly, hydrogenation and halogenation have been a powerful tool to induce large-gap QSH states in group-IV and V MLs [55,91]. Based on first-principles calculations, we show in Fig. 4 that the λ_{SO} and U in MLs BiAs can be tuned by the surface decoration, giving either a QSH or a QVH insulator. The structures of the hydrogenated (BiAsH_2) and halogenated (BiAsI_2) BiAs MLs are shown in Fig. 4(a). From the calculated bands and $\Omega(\mathbf{k})$ in Figs. 4(b) and (c), we see the desired difference between BiAsH_2 and BiAsI_2 . While the first is a QVH insulator with a trivial gap of

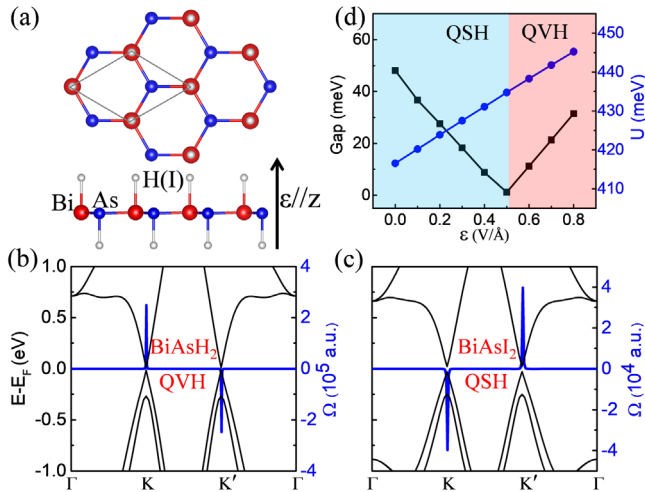


FIG. 4. (a) Top and side views of the MLs BiAsH₂ or BiAsI₂. (b),(c) Bands (black) with Berry curvatures (blue) for MLs BiAsH₂ and BiAsI₂. (d) Electric-field dependent gap in a ML BiAsI₂.

26 meV, $Z_2 = 0$, and $\Omega(\mathbf{k}) \neq \mathbf{0}$ at K and K' , the second BiAsI₂ is a QSH insulator with a nontrivial gap of 49 meV, $Z_2 = 1$, and reversed $\Omega(\mathbf{k})$. When two such MLs form a junction [Fig. 1], the QSVHK state can emerge along its interface. With hydrogenated and halogenated graphene routinely fabricated [92,93], the BiAsH₂-BiAsI₂ junction could be obtained from ML BiAs to support the QSVHK state by using the spatially selective growth and stencil lithography [71]. Since the electric field ϵ can directly change U in 2D materials [21,23], we also explore the possibility of an ϵ -controlled QSVHK state. Figure 4(d) shows that for ϵ applied along the z direction in ML BiAsI₂, U is increased and the gap is closed when $\epsilon = 0.5$ V/Å, the value achievable with ion-liquid gating [94,95]. Such a gap closing indicates a topological transition from QSH to QVH. Thus, the electric field can also be used to generate and control the QSVHK state.

With experimental realization of the QSVHK state, it would be possible to verify the inherent robustness of quantized conductance of spin-polarized channels, in contrast to QSH insulators, where this quantization is fragile even at He temperatures [80,81]. Furthermore, the QSVHK state offers an intriguing opportunity to study its manifestations of topological superconductivity through proximity effects [81,88,96] and test the related role of disorder [97,98].

We thank Professor Fan Zhang for fruitful discussions. This work is mainly supported by the U.S. DOE, Office of Science BES, Award No. DE-SC0004890 (T. Z. and I. Ž.), the National Basic Research Program of China under Grant No. 2019YFA0308403 (H. J.), the NSFC under Grants No. 11874298 (S. C.), 11822407 (H. J.), 11874117 (Z. Y.),

and 11574051 (Z. Y.), the German Federal Ministry of Education and Research (BMBF) via the Quantum Future project “MajoranaChips” (Grant No. 13N15264) within the funding program Photonic Research Germany (M. S. and P. S.) and the UB Center for Computational Research.

*Corresponding author.

tzhou8@buffalo.edu

[†]Corresponding author.

zigor@buffalo.edu

- [1] F. D. M. Haldane, Model for a Quantum Hall Effect without Landau Levels: Condensed-Matter Realization of the “Parity Anomaly”, *Phys. Rev. Lett.* **61**, 2015 (1988).
- [2] C. L. Kane and E. J. Mele, Z_2 Topological Order and the Quantum Spin Hall Effect, *Phys. Rev. Lett.* **95**, 146802 (2005).
- [3] J. Sichau, M. Prada, T. Anlauf, T. J. Lyon, B. Bosnjak, L. Tiemann, and R. H. Blick, Resonance Microwave Measurements of an Intrinsic Spin-Orbit Coupling Gap in Graphene: A Possible Indication of a Topological State, *Phys. Rev. Lett.* **122**, 046403 (2019).
- [4] X. Xu, W. Yao, D. Xiao, and T. F. Heinz, Spin and pseudospins in layered transition metal dichalcogenides, *Nat. Phys.* **10**, 343 (2014).
- [5] I. Žutić, J. Fabian, and S. Das Sarma, Spintronics: Fundamentals and applications, *Rev. Mod. Phys.* **76**, 323 (2004).
- [6] F. Reis, G. Li, L. Dudy, M. Bauernfeind, S. Glass, W. Hanke, R. Thomale, J. Schäfer, and R. Claessen, Bismuthene on a SiC substrate: A candidate for a high-temperature quantum spin Hall material, *Science* **357**, 287 (2017).
- [7] D. Xiao, W. Yao, and Q. Niu, Valley-Contrasting Physics in Graphene: Magnetic Moment and Topological Transport, *Phys. Rev. Lett.* **99**, 236809 (2007).
- [8] Z. Qiao, W.-K. Tse, H. Jiang, Y. Yao, and Q. Niu, Two-dimensional Topological Insulator State and Topological Phase Transition in Bilayer Graphene, *Phys. Rev. Lett.* **107**, 256801 (2011).
- [9] E. McCann and M. Koshino, The electronic properties of bilayer graphene, *Rep. Prog. Phys.* **76**, 056503 (2013).
- [10] R. V. Gorbachev, J. C. W. Song, G. L. Yu, A. V. Kretinin, F. Withers, Y. Cao, A. Mishchenko, I. V. Grigorieva, K. S. Novoselov, L. S. Levitov, and A. K. Geim, Detecting topological currents in graphene superlattices, *Science* **346**, 448 (2014).
- [11] M. Sui, G. Chen, L. Ma, W.-Y. Shan, D. Tian, K. Watanabe, T. Taniguchi, X. Jin, W. Yao, D. Xiao, and Y. Zhang, Gate-tunable topological valley transport in bilayer graphene, *Nat. Phys.* **11**, 1027 (2015).
- [12] Y. Shimazaki, M. Yamamoto, I. V. Borzenets, K. Watanabe, T. Taniguchi, and S. Tarucha, Generation and detection of pure valley current by electrically induced Berry curvature in bilayer graphene, *Nat. Phys.* **11**, 1032 (2015).
- [13] D. Xiao, G.-B. Liu, W. Feng, X. Xu, and W. Yao, Coupled Spin and Valley Physics in Monolayers of MoS₂ and Other Group-VI Dichalcogenides, *Phys. Rev. Lett.* **108**, 196802 (2012).

- [14] K. F. Mak, K. L. McGill, J. Park, and P. L. McEuen, The valley Hall effect in MoS₂ transistors, *Science* **344**, 1489 (2014).
- [15] I. Martin, Y. M. Blanter, and A. F. Morpurgo, Topological Confinement in Bilayer Graphene, *Phys. Rev. Lett.* **100**, 036804 (2008).
- [16] J. Jung, F. Zhang, Z. Qiao, and A. H. MacDonald, Valley-Hall kink and edge states in multilayer graphene, *Phys. Rev. B* **84**, 075418 (2011).
- [17] Z. Qiao, J. Jung, Q. Niu, and A. H. MacDonald, Electronic highways in bilayer graphene, *Nano Lett.* **11**, 3453 (2011).
- [18] A. Vaezi, Y. Liang, D. H. Ngai, L. Yang, and E.-A. Kim, Topological Edge States at a Tilt Boundary in Gated Multilayer Graphene, *Phys. Rev. X* **3**, 021018 (2013).
- [19] F. Zhang, A. H. MacDonald, and E. J. Mele, Valley Chern numbers and boundary modes in gapped bilayer graphene, *Proc. Natl. Acad. Sci. U.S.A.* **110**, 10546 (2013).
- [20] L. Ju, Z. Shi, N. Nair, Y. Lv, C. Jin, J. Velasco Jr, C. Ojeda-Aristizabal, H. A. Bechtel, M. C. Martin, A. Zettl, J. Analytis, and F. Wang, Topological valley transport at bilayer graphene domain walls, *Nature (London)* **520**, 650 (2015).
- [21] J. Li, K. Wang, K. J. McFaul, Z. Zern, Y. Ren, K. Watanabe, T. Taniguchi, Z. Qiao, and J. Zhu, Gate-controlled topological conducting channels in bilayer graphene, *Nat. Nanotechnol.* **11**, 1060 (2016).
- [22] L.-J. Yin, H. Jiang, J.-B. Qiao, and L. He, Direct imaging of topological edge states at a bilayer graphene domain wall, *Nat. Commun.* **7**, 11760 (2016).
- [23] J. Li, R.-X. Zhang, Z. Yin, J. Zhang, K. Watanabe, T. Taniguchi, C. Liu, and J. Zhu, A valley valve and electron beam splitter, *Science* **362**, 1149 (2018).
- [24] H. Chen, P. Zhou, J. Liu, J. Qiao, B. Oozyilmaz, and J. Martin, Gate controlled valley polarizer in bilayer graphene, *Nat. Commun.* **11**, 1202 (2020).
- [25] G. W. Semenoff, V. Semenoff, and F. Zhou, Domain Walls in Gapped Graphene, *Phys. Rev. Lett.* **101**, 087204 (2008).
- [26] Y. Kim, K. Choi, J. Ihm, and H. Jin, Topological domain walls and quantum valley Hall effects in silicene, *Phys. Rev. B* **89**, 085429 (2014).
- [27] S.-G. Cheng, H. Liu, H. Jiang, Q.-F. Sun, and X. C. Xie, Manipulation and Characterization of the Valley-Polarized Topological Kink States in Graphene-Based Interferometers, *Phys. Rev. Lett.* **121**, 156801 (2018).
- [28] C. Hu, V. Michaud-Rioux, W. Yao, and H. Guo, Moiré Valleytronics: Realizing Dense Arrays of Topological Helical Channels, *Phys. Rev. Lett.* **121**, 186403 (2018).
- [29] Z. Wang, S. Cheng, X. Liu, and H. Jiang, Topological kink states in graphene, *Nanotechnology* **32**, 402001 (2021).
- [30] S.-Q. Shen, *Topological Insulators: Dirac Equation in Condensed Matters* (Springer, Berlin, 2012).
- [31] G. Junker, *Supersymmetric Methods in Quantum and Statistical Physics* (Springer, Berlin, 1996).
- [32] R. Jackiw and C. Rebbi, Solitons with fermion number 1/2, *Phys. Rev. D* **13**, 3398 (1976).
- [33] W. P. Su, J. R. Schrieffer, and A. J. Heeger, Solitons in Polyacetylene, *Phys. Rev. Lett.* **42**, 1698 (1979).
- [34] I. Adagideli, P. M. Goldbart, A. Shnirman, and A. Yazdani, Low-Energy Quasiparticle States near Extended Scatterers in *d*-Wave Superconductors and Their Connection with SUSY Quantum Mechanics, *Phys. Rev. Lett.* **83**, 5571 (1999).
- [35] K. Sengupta, I. Žutić, H.-J. Kwon, V. M. Yakovenko, and S. Das Sarma, Midgap edge states and pairing symmetry of quasi-one-dimensional organic superconductors, *Phys. Rev. B* **63**, 144531 (2001).
- [36] D.-H. Lee, G.-M. Zhang, and T. Xiang, Edge Solitons of Topological Insulators and Fractionalized Quasiparticles in Two Dimensions, *Phys. Rev. Lett.* **99**, 196805 (2007).
- [37] Y. Nishida, L. Santos, and C. Chamon, Topological superconductors as nonrelativistic limits of Jackiw-Rossi and Jackiw-Rebbi models, *Phys. Rev. B* **82**, 144513 (2010).
- [38] K. Yasuda, M. Mogi, R. Yoshimi, A. Tsukazaki, K. Takahashi, M. Kawasaki, F. Kagawa, and Y. Tokura, Quantized chiral edge conduction on domain walls of a magnetic topological insulator, *Science* **358**, 1311 (2017).
- [39] M. Sedlmayr, N. Sedlmayr, J. Barnaś, and V. K. Dugaev, Chiral Hall effect in the kink states in topological insulators with magnetic domain walls, *Phys. Rev. B* **101**, 155420 (2020).
- [40] H. Pan, Z. Li, C.-C. Liu, G. Zhu, Z. Qiao, and Y. Yao, Valley-polarized Quantum Anomalous Hall Effect in Silicene, *Phys. Rev. Lett.* **112**, 106802 (2014).
- [41] T. Zhou, J. Zhang, B. Zhao, H. Zhang, and Z. Yang, Quantum spin-quantum anomalous Hall insulators and topological transitions in functionalized Sb (111) monolayers, *Nano Lett.* **15**, 5149 (2015).
- [42] T. Zhou, J. Zhang, Y. Xue, B. Zhao, H. Zhang, H. Jiang, and Z. Yang, Quantum spin-quantum anomalous Hall effect with tunable edge states in Sb monolayer-based heterostructures, *Phys. Rev. B* **94**, 235449 (2016).
- [43] J. Zhou, Q. Sun, and P. Jena, Valley-Polarized Quantum Anomalous Hall Effect in Ferrimagnetic Honeycomb Lattices, *Phys. Rev. Lett.* **119**, 046403 (2017).
- [44] M. Tahir, A. Manchon, K. Sabeeh, and U. Schwingenschlögl, Quantum spin/valley Hall effect and topological insulator phase transitions in silicene, *Appl. Phys. Lett.* **102**, 162412 (2013).
- [45] H. Huang, Z. Wang, N. Luo, Z. Liu, R. Lü, J. Wu, and W. Duan, Time-reversal symmetry protected chiral interface states between quantum spin and quantum anomalous Hall insulators, *Phys. Rev. B* **92**, 075138 (2015).
- [46] R. Banerjee, S. Mandal, and T. C. H. Liew, Optically induced topological spin-valley Hall effect for exciton polaritons, *Phys. Rev. B* **103**, L201406 (2021).
- [47] X.-L. Qi and S.-C. Zhang, Topological insulators and superconductors, *Rev. Mod. Phys.* **83**, 1057 (2011).
- [48] S. F. Islam and C. Benjamin, A scheme to realize the quantum spin-valley Hall effect in monolayer graphene, *Carbon* **110**, 304 (2016).
- [49] A. Dyrdął and J. Barnaś, Anomalous, spin, and valley Hall effects in graphene deposited on ferromagnetic substrates, *2D Mater.* **4**, 034003 (2017).
- [50] T. Zhou, J. Zhang, H. Jiang, I. Žutić, and Z. Yang, Giant spin-valley polarizations and multiple Hall effects in functionalized bismuth monolayers, *npj Quantum Mater.* **3**, 39 (2018).

- [51] S. Zhang, S. Guo, Z. Chen, Y. Wang, H. Gao, J. Gómez-Herrero, P. Ares, F. Zamora, Z. Zhu, and H. Zeng, Recent progress in 2D group-VA semiconductors: from theory to experiment, *Chem. Soc. Rev.* **47**, 982 (2018).
- [52] R. Gui, H. Jin, Y. Sun, X. Jiang, and Z. Sun, Two-dimensional group-VA nanomaterials beyond black phosphorus: Synthetic methods, properties, functional nanostructures and applications, *J. Mater. Chem. A* **7**, 25712 (2019).
- [53] J. Ji, X. Song, J. Liu, Z. Yan, C. Huo, S. Zhang, M. Su, L. Liao, W. Wang, Z. Ni, Y. Hao, and H. Zeng, Two-dimensional antimonene single crystals grown by van der Waals epitaxy, *Nat. Commun.* **7**, 13352 (2016).
- [54] G. Xu, T. Zhou, B. Scharf, and I. Žutić, Optically Probing Tunable Band Topology in Atomic Monolayers, *Phys. Rev. Lett.* **125**, 157402 (2020).
- [55] Z. Song, C.-C. Liu, J. Yang, J. Han, M. Ye, B. Fu, Y. Yang, Q. Niu, J. Lu, and Y. Yao, Quantum spin Hall insulators and quantum valley Hall insulators of BiX/SbX (X = H, F, Cl and Br) monolayers with a record bulk band gap, *NPG Asia Mater.* **6**, e147 (2014).
- [56] Z. Liu, W. Feng, H. Xin, Y. Gao, P. Liu, Y. Yao, H. Weng, and J. Zhao, Two-dimensional spin-valley-coupled Dirac semimetals in functionalized SbAs monolayers, *Mater. Horizon* **6**, 781 (2019).
- [57] S.-S. Li, W.-X. Ji, P. Li, S.-J. Hu, T. Zhou, C.-W. Zhang, and S.-S. Yan, Unconventional band inversion and intrinsic quantum spin Hall effect in functionalized group-V binary films, *Sci. Rep.* **7**, 6126 (2017).
- [58] Y. Ren, Z. Qiao, and Q. Niu, Topological phases in two-dimensional materials: A review, *Rep. Prog. Phys.* **79**, 066501 (2016).
- [59] O. Ávalos-Ovando, D. Mastrogiovanni, and S. E. Ulloa, Lateral interfaces of transition metal dichalcogenides: A stable tunable one-dimensional physics platform, *Phys. Rev. B* **99**, 035107 (2019).
- [60] H. Pan, X. Li, F. Zhang, and S. A. Yang, Perfect valley filter in a topological domain wall, *Phys. Rev. B* **92**, 041404(R) (2015).
- [61] S. Das Sarma, S. Adam, E. H. Hwang, and E. Rossi, Electronic transport in two-dimensional graphene, *Rev. Mod. Phys.* **83**, 407 (2011).
- [62] S. Datta, *Electronic Transport in Mesoscopic Systems* (Cambridge University Press, Cambridge, England, 1997).
- [63] M. P. L. Sancho, J. L. Sancho, and J. Rubio, Quick iterative scheme for the calculation of transfer matrices: application to Mo (100), *J. Phys. F* **14**, 1205 (1984).
- [64] H. Jiang, L. Wang, Q.-F. Sun, and X. C. Xie, Numerical study of the topological Anderson insulator in HgTe/CdTe quantum wells, *Phys. Rev. B* **80**, 165316 (2009).
- [65] Z. Qiao, Y. Han, L. Zhang, K. Wang, X. Deng, H. Jiang, S. A. Yang, J. Wang, and Q. Niu, Anderson Localization from the Berry-Curvature Interchange in Quantum Anomalous Hall Systems, *Phys. Rev. Lett.* **117**, 056802 (2016).
- [66] S.-G. Cheng, R.-Z. Zhang, J. Zhou, H. Jiang, and Q.-F. Sun, Perfect valley filter based on a topological phase in a disordered Sb monolayer heterostructure, *Phys. Rev. B* **97**, 085420 (2018).
- [67] P. W. Anderson, Absence of diffusion in certain random lattices, *Phys. Rev.* **109**, 1492 (1958).
- [68] C. G. Montgomery, J. I. Krugler, and R. M. Stubbs, Green's-Function Theory of a Disordered Heisenberg Ferromagnet, *Phys. Rev. Lett.* **25**, 669 (1970).
- [69] A. Rycerz, J. Tworzydło, and C. W. J. Beenakker, Anomalously large conductance fluctuations in weakly disordered graphene, *Europhys. Lett.* **79**, 57003 (2007).
- [70] S.-G. Cheng, J. Zhou, H. Jiang, and Q.-F. Sun, The valley filter efficiency of monolayer graphene and bilayer graphene line defect model, *New J. Phys.* **18**, 103024 (2016).
- [71] See Supplemental Material, which includes Refs. [72–79], at <http://link.aps.org/supplemental/10.1103/PhysRevLett.127.116402> for first-principles calculation methods, fabrication details, expanded discussion of the conductance calculations with disorder, and the influence of the Rashba spin-orbit coupling, temperature, and interface configurations.
- [72] G. Kresse and J. Furthmüller, Efficient iterative schemes for ab initio total-energy calculations using a plane-wave basis set, *Phys. Rev. B* **54**, 11169 (1996).
- [73] J. P. Perdew, K. Burke, and M. Ernzerhof, Generalized Gradient Approximation Made Simple, *Phys. Rev. Lett.* **77**, 3865 (1996).
- [74] Y. Yao, L. Kleinman, A. H. MacDonald, J. Sinova, T. Jungwirth, D.-S. Wang, E. Wang, and Q. Niu, First Principles Calculation of Anomalous Hall Conductivity in Ferromagnetic bcc Fe, *Phys. Rev. Lett.* **92**, 037204 (2004).
- [75] Q. Wu, S. Zhang, H.-F. Song, M. Troyer, and A. A. Soluyanov, WannierTools: An open-source software package for novel topological materials, *Comput. Phys. Commun.* **224**, 405 (2018).
- [76] X. Ni, H. Huang, and F. Liu, Robustness of topological insulating phase against vacancy, vacancy cluster, and grain boundary bulk defects, *Phys. Rev. B* **101**, 125114 (2020).
- [77] C. Xu and J. E. Moore, Stability of the quantum spin Hall effect: Effects of interactions, disorder, and Z_2 topology, *Phys. Rev. B* **73**, 045322 (2006).
- [78] J. C. Budich, F. Dolcini, P. Recher, and B. Trauzettel, Phonon-Induced Backscattering in Helical Edge States, *Phys. Rev. Lett.* **108**, 086602 (2012).
- [79] E. S. Walker, S. Muschinske, C. J. Brennan, S. R. Na, T. Trivedi, S. D. March, Y. Sun, T. Yang, A. Yau, D. Jung, A. F. Briggs, E. M. Krivoy, M. L. Lee, K. M. Liechti, E. T. Yu, D. Akinwande, and S. R. Bank, Composition-dependent structural transition in epitaxial $\text{Bi}_{1-x}\text{Sb}_x$ thin films on Si(111), *Phys. Rev. Mater.* **3**, 064201 (2019).
- [80] M. König, S. Wiedmann, C. Brüne, A. Roth, H. Buhmann, L. W. Molenkamp, X.-L. Qi, and S.-C. Zhang, Quantum spin Hall insulator state in HgTe quantum wells, *Science* **318**, 766 (2007).
- [81] D. Culcer, A. Cem Keser, Y. Li, and G. Tkachov, Transport in two-dimensional topological materials: Recent developments in experiment and theory, *2D Mater.* **7**, 022007 (2020).
- [82] G. Li, W. Hanke, E. M. Hankiewicz, F. Reis, J. Schäfer, R. Claessen, C. Wu, and R. Thomale, Theoretical paradigm for the quantum spin Hall effect at high temperatures, *Phys. Rev. B* **98**, 165146 (2018).

- [83] D. Hsieh, D. Qian, L. Wray, Y. Xia, Y. S. Hor, R. J. Cava, and M. Z. Hasan, A topological Dirac insulator in a quantum spin Hall phase, *Nature (London)* **452**, 970 (2008).
- [84] H. Huang, K.-H. Jin, and F. Liu, Alloy Engineering of Topological Semimetal Phase Transition in $MgTa_{2-x}Nb_xN_3$, *Phys. Rev. Lett.* **120**, 136403 (2018).
- [85] P. Schüffelgen *et al.*, Selective area growth and stencil lithography for in situ fabricated quantum devices, *Nat. Nanotechnol.* **14**, 825 (2019).
- [86] M.-S. Chen, S. L. Brandow, T. L. Schull, D. B. Chrisey, and W. J. Dressick, A non-covalent approach for depositing spatially selective materials on surfaces, *Adv. Funct. Mater.* **15**, 1364 (2005).
- [87] H. Dery, Y. Song, P. Li, and I. Žutić, Silicon spin communications, *Appl. Phys. Lett.* **99**, 082502 (2011).
- [88] I. Žutić, A. Matos-Abiague, B. Scharf, H. Dery, and K. Belashchenko, Proximity-induced materials, *Mater. Today* **22**, 85 (2019).
- [89] M. Lindemann, G. Xu, T. Pusch, R. Michalzik, M. R. Hofmann, I. Žutić, and N. C. Gerhardt, Ultrafast spin-lasers, *Nature (London)* **568**, 212 (2019).
- [90] A. J. Mannix, B. Kiraly, M. C. Hersam, and N. P. Guisinger, Synthesis and chemistry of elemental 2D materials, *Nat. Rev. Chem.* **1**, 0014 (2017).
- [91] Y. Xu, B. Yan, H.-J. Zhang, J. Wang, G. Xu, P. Tang, W. Duan, and S.-C. Zhang, Large-Gap Quantum Spin Hall Insulators in Tin Films, *Phys. Rev. Lett.* **111**, 136804 (2013).
- [92] R. Balog, B. Jørgensen, L. Nilsson, M. Andersen, E. Riens, M. Bianchi, M. Fanetti, E. Laegsgaard, A. Baraldi, S. Lizzit, Z. Sljivancanin, F. Besenbacher, B. Hammer, T. G. Pedersen, P. Hofmann, and L. Hornekaer, Bandgap opening in graphene induced by patterned hydrogen adsorption, *Nat. Mater.* **9**, 315 (2010).
- [93] F. Karlický, K. Kumara Ramanatha Datta, M. Otyepka, and R. Zbořil, Halogenated graphenes: Rapidly growing family of graphene derivatives, *ACS Nano* **7**, 6434 (2013).
- [94] A. Hebard, A. Fiory, and R. Eick, Experimental considerations in the quest for a thin-film superconducting field-effect transistor, *IEEE Trans. Magn.* **23**, 1279 (1987).
- [95] J. Mannhart, J. Ströbel, J. G. Bednorz, and C. Gerber, Large electric field effects in $YBa_2Cu_3O_{7-\delta}$ films containing weak links, *Appl. Phys. Lett.* **62**, 630 (1993).
- [96] L. Fu and C. L. Kane, Superconducting Proximity Effect and Majorana Fermions at the Surface of a Topological Insulator, *Phys. Rev. Lett.* **100**, 096407 (2008).
- [97] I. Adagideli, M. Wimmer, and A. Teker, Effects of electron scattering on the topological properties of nanowires: Majorana fermions from disorder and superlattices, *Phys. Rev. B* **89**, 144506 (2014).
- [98] A. Habibi, S. A. Jafari, and S. Rouhani, Resilience of Majorana fermions in the face of disorder, *Phys. Rev. B* **98**, 035142 (2018).

Quantum Spin-Valley Hall Kink States: From Concept to Material Design

Tong Zhou¹, Shuguang Cheng², Michael Schleienvoigt³, Peter Schüelgen³,
Hua Jiang⁴, Zhongqin Yang⁵, and Igor Žutić¹

¹Department of Physics, University at Buffalo, SUNY, Buffalo, NY 14260, USA

²Department of Physics, Northwest University, Xi'an 710069, China

³Peter Grünberg Institute 9, Forschungszentrum Jülich & JARA Jülich-Aachen Research Alliance, 52425 Jülich, Germany

⁴School of Physical Science and Technology, Soochow University, Suzhou 215006, China

⁵State Key Laboratory of Surface Physics and Key Laboratory of Computational Physical Sciences (MOE) and Department of Physics and Collaborative Innovation Center of Advanced Microstructures, Fudan University, Shanghai 200433, China

I. First-Principles Calculation Methods and Orbital-Resolved Bands

II. Conductance Calculations

III. Rashba Spin-Orbit Coupling

IV. Influence and Crossover of the Short-range and Long-range Disorder

V. Influence of the Interface Configuration

VI. Influence of the Temperature

VII. Experimental Fabrication

VIII. Influence of the Stoichiometry

I. First-Principles Calculation Methods and Orbital-Resolved Bands

The geometry optimization and electronic structure calculations were performed by using the first-principles method based on density-functional theory (DFT) with the projector-augmented-wave (PAW) formalism, as implemented in the Vienna ab-initio simulation package (VASP) [1]. All calculations were carried out with a plane-wave cutoff energy of 550 eV and $12 \times 12 \times 1$ Monkhorst-Pack grids were adopted for the first Brillouin zone integral. The Perdew-Burke-Ernzerhof generalized-gradient approximation (GGA) was used to describe the exchange and correlation functional [2]. A vacuum space of larger than 15 Å was used to avoid the interaction between two adjacent slabs. The convergence criterion for the total energy is 10^{-6} eV. The conjugated gradient algorithm is employed to perform the structural optimization. All the atoms in the unit cell are allowed to move until the Hellmann–Feynman force on each atom is smaller than 0.01 eV/Å. The lattice constants of Bi/SiC, BiAs/SiC and BiSb/SiC are 5.35 Å, taken from the experiments [3]. The optimized lattice constants of BiAsH₂ and BiAsI₂ are 5.07 Å and 5.08 Å, respectively. The Berry curvature, $\Omega(\mathbf{k})$ for the whole valence bands are calculated by [4]

$$\Omega(\mathbf{k}) = \sum_n f_n \Omega_n(\mathbf{k}),$$

$$\Omega_n(\mathbf{k}) = -2 \operatorname{Im} \sum_{m \neq n} \frac{\langle \psi_{n\mathbf{k}} | v_x | \psi_{m\mathbf{k}} \rangle \langle \psi_{m\mathbf{k}} | v_y | \psi_{n\mathbf{k}} \rangle \hbar^2}{(E_m - E_n)^2},$$

where E_n is the eigenvalue of the Bloch functions $|\psi_{n\mathbf{k}}\rangle$, f_n is the Fermi-Dirac distribution function at zero temperature, v_x and v_y are the velocity operators. The Z₂ invariant was computed by tracing the Wannier charge centers using the non-Abelian Berry connection as implemented in the WannierTools software [5].

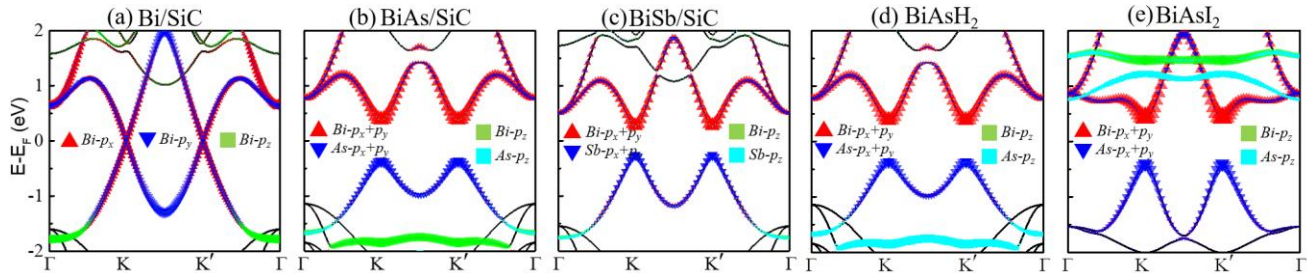


Fig. S1 (a)-(e) Orbital-resolved bands without SOC for Bi/SiC, BiSb/SiC, BiAs/SiC, BiAsH₂ and BiAsI₂ monolayers, respectively.

The orbital-resolved bands without spin-orbit coupling (SOC) of Bi/SiC, BiAs/SiC, BiSb/SiC, BiAsH₂, and BiAsI₂ are shown in Fig. S1, where we can clearly see all their bands near the Fermi level are dominated by the p_x and p_y orbitals of Bi, Sb, or As atoms, indicating their low energy electronic structures and topological properties can be well described by our tight-binding (TB) model based on p_x and p_y basis. By fitting the TB model with DFT calculated bands, the intrinsic SOC and staggered potential (λ_{SO} , U) for Bi/SiC, BiAs/SiC, BiSb/SiC, BiAsH₂, and BiAsI₂ are obtained as (0.44 eV, 0 eV), (0.24 eV, 0.38 eV), (0.30 eV, 0.26 eV), (0.35 eV, 0.37 eV), and (0.44 eV, 0.41 eV), respectively.

II. Conductance Calculations

The conductance of the quantum spin Hall (QSH), quantum-valley Hall kink (QVHK), and quantum-spin-valley Hall kink (QSVHK) states are calculated by employing a two-terminal Landauer-Büttiker formalism based on the Green function technique [6]

$$G_{LR} = \frac{e^2}{h} \text{Tr}[\Gamma_L G' \Gamma_R G^a],$$

where $G^{r(a)}$ is the retarded (advanced) Green function of the central scattering region, as shown in Fig. S2(a). The terminals are assumed the same as the central region in the absence of disorder. The quantities $\Gamma_{L(R)} = i[\sum_{L(R)}^r - \sum_{L(R)}^a]$ are the linewidth functions describing the coupling between the left (right) terminal and the central scattering region, where $\Sigma^{r(a)}$ is the retarded (advanced) self-energy due to the L(R) semi-infinite lead, and can be numerically obtained via a transfer matrix method [7].

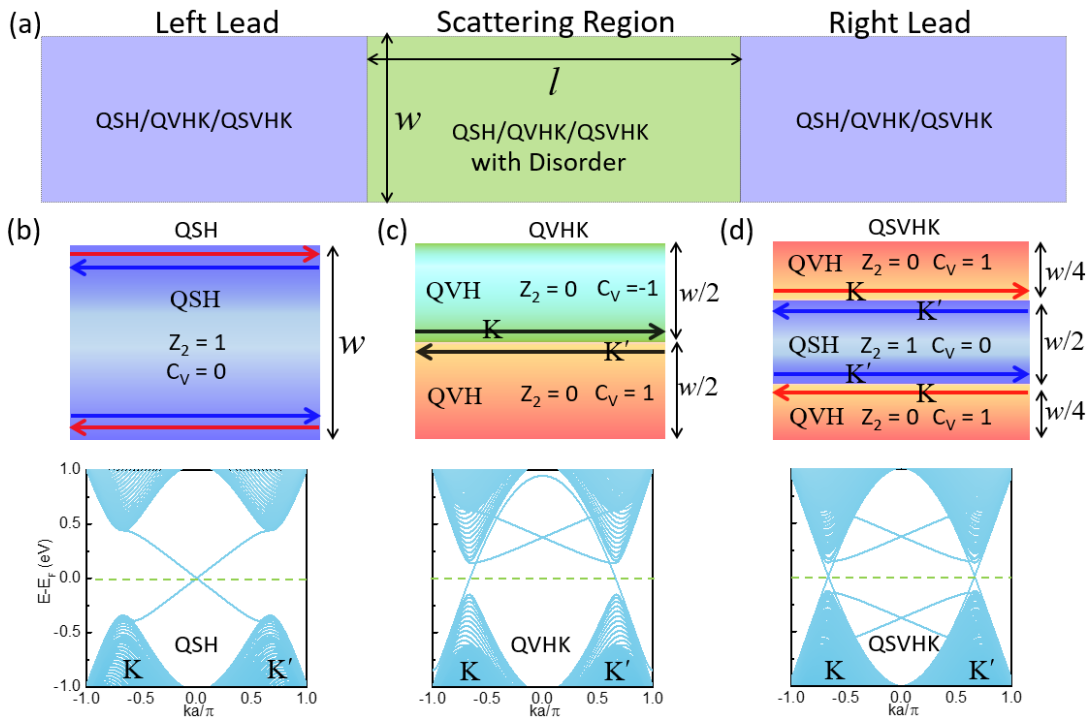


Fig. S2 (a) Two-terminal model for conductance calculations. (b)-(c) The schematic (top) and calculated bands (bottom) for QSH, QVHK and QSVHK states, respectively. The parameters (λ_{SO} , U) of (0.44 eV, 0 eV), (0.24 eV, 0.38 eV) and (0.24 eV, -0.38 eV) obtained from Bi/SiC, BiAs/SiC, and AsBi/SiC, are used for QSH, QVH ($C_V=1$), and QVH ($C_V=-1$) regions. The length (l) and width (w) of the scattering region are 100 and 200 unit cells, corresponding to 46 nm and 92 nm, respectively. The hopping parameter $t_{1,2}$ is set to be 1 eV.

For the QSH states, the conductance calculations are based on the bands of Bi/SiC in Fig. S2(b). For QVHK states, we construct a BiAs-AsBi/SiC junction with $C_V = 1$ (-1) in the BiAs/SiC (AsBi/SiC) region, where the spin-degenerate kink states appear along the interface as shown in Fig. S2(c). The conductance of the QSVHK states is calculated based on the BiAs-Bi-BiAs/SiC junction as shown in Fig. S2(d). The Fermi level, E_F is 0 in all conductance calculations. The disorder is added in the scattering region (See details in Sec. IV). For each value of the disorder strength, 200 disorder configurations are averaged.

III. Rashba Spin-Orbit Coupling

Considering Rashba SOC can be induced into bismuthene by the SiC substrate [3], here we explore its influence on QSVHK states. The Rashba SOC in Bi/SiC is described by H_R based on a TB model in the basis of p_x and p_y orbitals with [3, 8, 9]

$$H_R = \sum_i \sum_{j=1,2,3} c_i^\dagger T_{R\delta_j} c_{i+\delta_j} + H.C.$$

Here, c_i represents the annihilation operator on site \mathbf{i} . $T_{R\delta}$ describes the nearest hopping from site \mathbf{i} to $\mathbf{i} + \delta_j$, which is induced by the extrinsic Rashba SOC from the SiC substrate with

$$T_{R\delta_j} = (-1)^{j+1} i \begin{bmatrix} \lambda_R & z^{(3-j)} \lambda'_R \\ z^j \lambda'_R & \lambda_R \end{bmatrix} \otimes [s_x \sin(\frac{3-j}{3})\pi - s_y \cos(\frac{3-j}{3})\pi],$$

where $z = \exp(2i\pi/3)$, λ_R and λ'_R reflect the Rashba SOC strength with $\lambda'_R = \lambda_R t_2/t_1$, and s indicates the Pauli matrices acting on the spin space. By fitting the TB bands including Rashba SOC with DFT calculated bands [Fig. 3], we obtain λ_R of 30 meV for Bi/SiC, which is consistent with the previous work [3]. Similarly, λ_R of 28 meV is obtained for BiAs/SiC system.

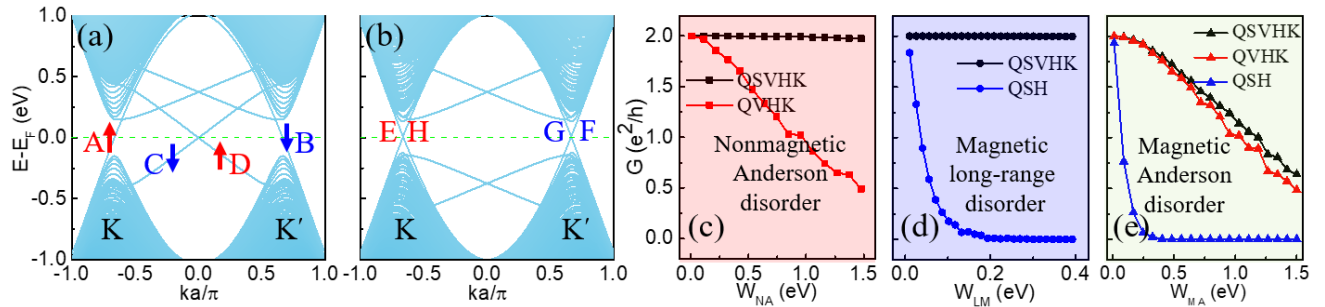


Fig. S3 (a) - (e) same as Figs. 2 (a) - (e), but with Rashba SOC of $\lambda_R = 30$ meV, respectively.

Since Rashba SOC does not change the valley-inversion symmetry (VIS) and time-reversal symmetry (TRS), and its strength λ_R is much smaller compared to U and λ_{SO} in the BiAs-Bi/SiC system, it is expected the Rashba SOC does not affect much the results. Indeed, as shown in Figs. S3(a) and (b), the bands with Rashba SOC are nearly the same as the corresponding bands without Rashba SOC [Figs. 2(a) and (b)]. Furthermore, there is no obvious difference between the QSVHK conductance with and without Rashba SOC in the presence of disorder, as shown in Figs. S3(c)-(e) compared to those in Figs. 2(c)-(e). Specifically, the conductance of QSVHK states remain quantized against the nonmagnetic Anderson disorder and magnetic long-range disorder with the consideration of Rashba SOC. Thus, it is reasonable to neglect the influence of Rashba SOC in QSVHK states for BiAs-Bi/SiC system.

IV. Influence and Crossover of the Short-Range and Long-Range Disorder

For valley-related transport, the influence of the short- and long-range disorder is usually significantly different since the former (latter) induces (excludes) intervalley scattering, which has been well explored in graphene [10]. The short (long)-range disorder is characterized by the smaller (larger) disorder correlation length, λ , compared to the lattice spacing, a [10, 11]. Their crossover can be well described by a Gaussian correlated disorder potential of $\eta(r) = \omega e^{-r^2/\lambda^2}$, where ω parametrizes the disorder strength [10, 11]. Specifically, for a short-range disorder, usually induced by the point defects [10], its disorder potential localizes in the atomic range ($\lambda < a$) and the induced intervalley scattering enables strong backscattering, eventually turning the conducting system into an Anderson insulator. Such a short-range disorder is also called Anderson disorder, when $\lambda \rightarrow 0$ [10, 11]. In contrast, for a long-range disorder, often arising from the charged impurities or ripples [10], its disorder potential is smooth on the scale of the lattice spacing ($\lambda > a$) and there is very little intervalley scattering. As a result, the back scattering is suppressed and the system remains highly conductive [10, 11].

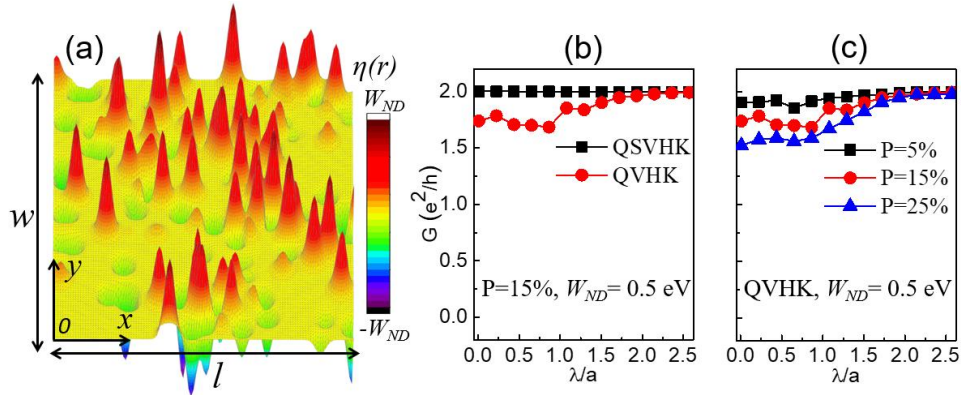


Fig. S4. (a) An example of a realization of the $\eta(r)$ in 2D system. (b) Conductance, G , as a function of the correlation length, λ , for the QVHK and QSVHK states with $\eta(r)$ as in (a), where the disorder probability $P = 15\%$ and the disorder strength $W_{ND} = 0.5$ eV. (c) Same as (b) but for QVHK with various P . In conductance calculations, the width (w) and length (l) of the scattering region are 120 and 2000 unit cells, respectively. Other parameters are taken from Fig. S2.

To explore the influence of the short-range and long-range disorder in our proposed QSVHK states, we add a nonmagnetic disorder term [12] $H_{ND} = \sum_i c_i^\dagger \eta_i \begin{bmatrix} 1 & 1 \\ 1 & 1 \end{bmatrix} \otimes \sigma_0 c_i$ to Eq. (1). Here, we rewrite $\eta(r)$ in a discrete

model as $\eta_i = \sum_{j=1}^{N_p} \omega_j e^{-|r_{ij}/\lambda|^2}$, where $|r_{ij}|$ is the distance between site i and j , N_p is the total number of the scattering centers, which, dividing the total number (N) of the lattice sites, gives the disorder probability, $P = N_p/N$. Figure S4(a) shows the realization of the $\eta(r_i)$. For the short-range disorder, we consider the Anderson disorder ($\lambda = 0$) with $P = 100\%$, where ω_j is randomly distributed in $[-W_{NA}, W_{NA}]$ with W_{NA} the nonmagnetic Anderson disorder strength. By employing Landauer-Büttiker formalism with the Green function technique in a two-terminal model as in Fig. S2, we calculate the QSVHK conductance, G , as a function of W_{NA} shown in Fig. 2(c) in the Main Text. For comparison, we also calculate $G(W_{NA})$ of QVHK states there. Since QVHK states require the absence of the intervalley scattering, it can only be robust against the long-range disorder. When there exists a short-range disorder, the valley inversion symmetry is broken and the intervalley scattering is easily induced. Thus, its conductance decreases from the quantization as shown in Fig. 2(c). For our proposed QSVHK, because of the additional protection from the QSH, it is not influenced by the intervalley scattering and thus remains robust against nonmagnetic short-range disorder [Fig. 2(c)].

To explore the crossover of the short-range and long-range disorder in the QSVHK, we induce the magnetic short/long-range disorder [13] to break the TRS and thus validating the intervalley scattering in the QSVHK. When the TRS is broken, the QSVHK degrades into the QVHK, and then it is expected to be robust against the magnetic long-range disorder, but can be intervalley-scattered by the magnetic short-range disorder. The magnetic disorder

is induced by adding an in-plane magnetic exchange filed $H_{MD} = \sum_i c_i^\dagger \eta_i \begin{bmatrix} 1 & 1 \\ 1 & 1 \end{bmatrix} \otimes \sigma_x c_i$ to Eq. (1). Similar to that

in nonmagnetic case, for the short-range disorder, we consider the magnetic Anderson disorder ($\lambda = 0$ and $P = 100\%$) with W_{MA} the magnetic Anderson disorder strength. While for the magnetic long-range disorder, we consider $\lambda = 7a$ and $P = 1\%$ with W_{LM} the magnetic long-range disorder strength. Through the conductance calculations, we find the QSVHK conductance remains quantized with W_{LM} [Fig. 2(d)], but decreases with W_{MA} [Fig. 2(e)], consistent with our expectations.

It is generally accepted that the critical disorder correlation length, $\lambda_c \sim a$, separates the short- and long-range disorder [10]. However, for a specific system, λ_c may also be related to the electronic structures of the system and the details of the disorder, including its strength and concentration. To identify the λ_c in our proposed bismuthene system, we calculate the QVHK conductance in the presence of the nonmagnetic disorder $\eta(r_i)$ with various λ as shown in Fig. S4(b), where the η is randomly distributed in $[-W_{NA}, W_{NA}]$ with W_{NA} the nonmagnetic disorder strength. We can see that for $\lambda < 2a$, $G < 2e^2/h$, indicating there is a finite intervalley scattering, while for $\lambda > 2a$, the conductance is quantized due to the vanishing intervalley scattering. Thus, λ_c is about $2a$ in bismuthene system with $P = 15\%$ and $W_{ND} = 0.5$ eV. λ_c is slightly increased when P increases, as shown in Fig. S4(c). This can be readily understood since the larger P enhances the possibility of the intervalley scattering, thus requiring a larger λ_c to compensate it.

V. Influence of the Interface Configuration

Based on the analysis of the topological charge, the QSVHK emerges as long as the topological indexes (Z_2 and C_v) change across the interface. Thus, the QSVHK is expected to be insensitive to the detailed interface configurations, reflecting its topological nature and protection. To clearly show such robustness against the interface configurations, we consider various interface situations discussed as follows, including the gradual interface, curved interface and the interfacial defects.

Influence of the gradual interface. In the Main Text, we assume that the QSH-QVH interface is very sharp, where the parameters (λ_{SO} , U) change as a step function. However, in experiments, because of the atom mixing, the interface may not be as sharp but instead form a domain wall (DW) with a finite width (w_D) as shown in Fig. S5(a). Such a DW can be described by a smooth change of the parameters, taking, for example, cosine change as shown in Figs. S5(b) and (c). Figures S5(d)-(f) show the calculated bands of the QVH-QSH-QVH junctions with various w_D . We can see their bands are quite similar and the QSVHK emerges in all cases, regardless of the DW width. However, the localization length of the QSVHK increases as w_D increases, as shown in the calculated spatial local density of the states (LDOS) of the QSVHK in Fig. S5(g), reflecting the DW character. Since the energy spectra are similar for various w_D , it is expected they also show similar transport properties. To verify this, we calculate their conductances based on a two-terminal model [Fig. S5(a)]. As shown in Fig. S5(h), in the clean limit, the conductance is large outside the bulk gap, while it equals to $2e^2/h$ within the gap. Such quantized conductance originates from the QSVHK. Similar $G(E)$ trends for various w_D indicate the transport properties of the QSVHK do not depend on the DW width.

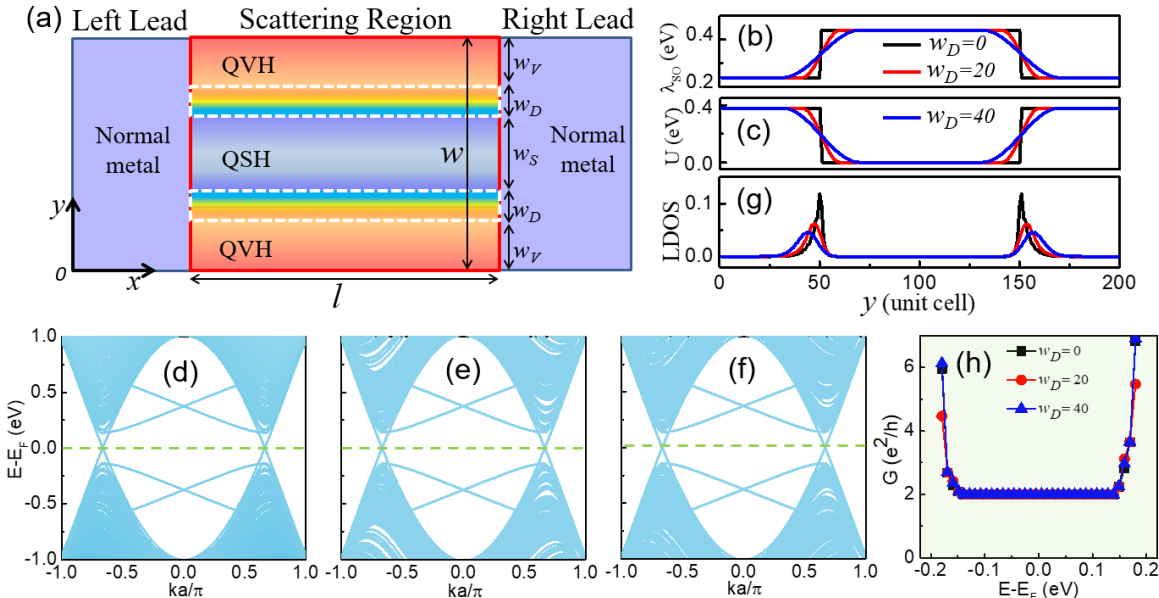


Fig. S5 (a) Two-terminal model for conductance calculations of the QVH-QSH-QVH junctions with domain walls, where w_V , w_S , and w_D indicate the width of the QVH region, QSH region, and domain wall (marked by the white dashed rectangle), respectively. (b) and (c) The parameters of (λ_{SO} , U) change from the QVH region to the QSH region as $\lambda_{SO} = \frac{\lambda_1 + \lambda_2}{2} + \frac{\lambda_1 - \lambda_2}{2} \cos\left(\frac{y-y_{L,R}+w_D}{2w_D}\pi\right)$ and $U = \frac{U_1 + U_2}{2} + \frac{U_1 - U_2}{2} \cos\left(\frac{y-y_{L,R}+w_D}{2w_D}\pi\right)$ with $y_{L,R} - w_D < y < y_{L,R} + w_D$, where $y_L = 50$ ($y_R = 150$) are the center of the left (right) domain walls, $\lambda_{1,2}$ and $U_{1,2}$ are the intrinsic SOC and staggered potential for the QVH and QSH region, taken from the BiAs/SiC and Bi/SiC, respectively. The $w_V = 50 - w_D/2$ and $w_S = 100 - w_D$. (d) - (f) Bands for the scattering region in (a) with $w_D = 0, 20, 40$ unit cells, respectively. (g) Spatial local density of states (LDOS) for the bands at E_F for (d)-(f). (h) Conductance, G , as a function of the energy E with various w_D for the setup in (a). The l is infinite in band calculations while $l = 200$ unit cells for conductance calculations. Other parameters are taken from Fig. S2 in SM.

Influence of the curved interface. Besides the DW width, the shape of the interface is another important interfacial property. Based on the topological analysis and index theorem, it is expected that the QSVHK states emerge exactly along the interface, regardless of its shape. To illustrate this, we design a curved QSH-QVH interface with sine feature as an example, as shown in Fig. S6(a). The calculated LDOS [Fig. S6(b)] show that the QSVHK exactly flows along the physical interface. Based on similar transport calculations as in Fig. S5, the obtained conductance of the curved interface [Fig. S6(c)] is found to be similar to that of the straight one [Fig. S5(h)]. Especially, the quantized conductance within the gap clearly demonstrates that QSVHK emerges in the curved boundary and its transport properties are insensitive to the shape of the interface.

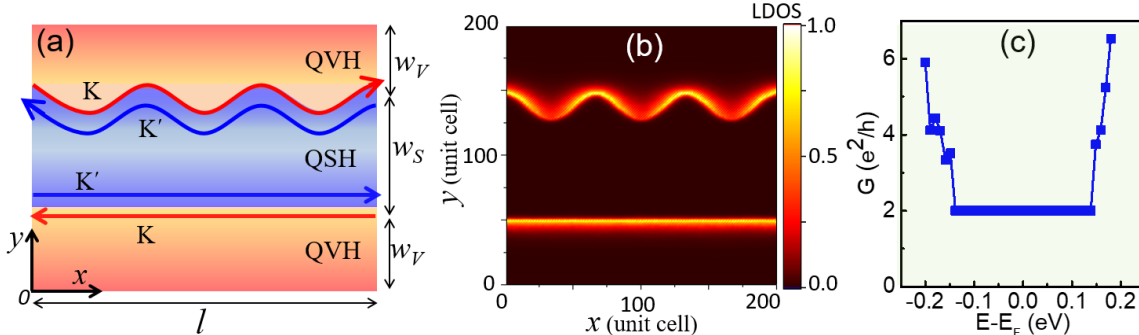


Fig. S6 (a) Schematic of QVH-QSH-QVH junctions with curved interface of $20[1-\cos(6\pi x/l)]$. (b) Spatial LDOS at E_F for the spectrum of (a). (c) Conductance, G , as a function of E for (a) with $l = 2w_S = 4w_V = 200$ unit cells. The parameters are taken from Fig. S5.

Influence of the interfacial defects. Considering the defects can be created around the interface when fabricating the junctions, here we explore the influence of the defects in QSVHK states. As we demonstrated in the Main Text, our proposed QSVHK states are topologically protected by both the valley-inversion and time reversal symmetries. As long as these two symmetries are not simultaneously broken, the QSVHK states can remain robust. As topological states, they are highly robust against the local defects and disorder. Considering the defects in the interface are locally distributed and cannot break the time-reversal symmetry [14, 15], the QSVHK states are expected to be robust against such defects. Encouragingly, a recent study shows even for global defects the quantum spin Hall (QSH) states in bismuthene remain robust when the defect concentration is lower than 17% [15]. Since our proposed QSVHK states are more robust than the QSH states because of the additional protection from the valley-inversion symmetry, the QSVHK states are expected to be robust against the defects.

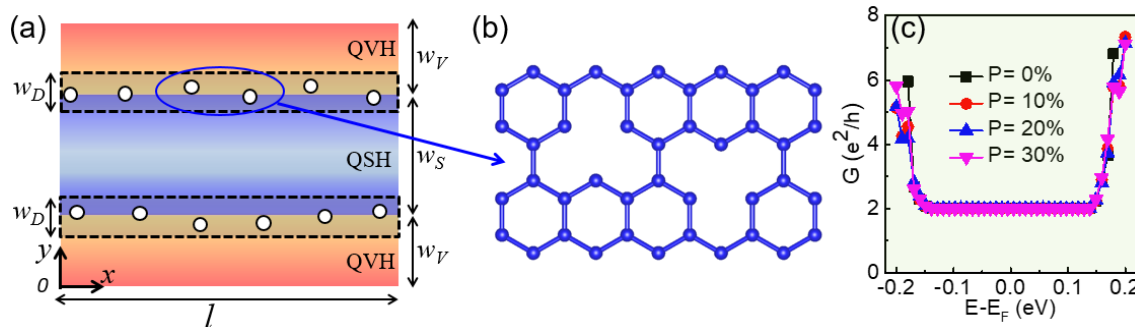


Fig. S7 (a) Schematic of QVH-QSH-QVH junctions with defects marked by the circles around the interface, where the defects are created by randomly removing the atoms in the black dashed rectangle regions with the width $w_D = 15$ unit cells. The concentration of the defects, P , is defined by the number of the removed atoms over the total number of the atoms in the black dashed rectangle regions. (b) The schematic of the atomic structures with defects for the zoom-in of the area marked by the blue circle in (a). (c) Conductance, G , as a function of E for (a) with various P based on the two-terminal model (Fig. S5), where $l = 2w_S = 4w_V = 200$ unit cells. The other parameters are taken from Fig. S5.

To check our expectations, we create the defects by randomly removing the atoms around the QSH-QVH interface as shown in Figs. S7(a)-(b). Based on similar transport calculations as in Fig. S5, we calculate the conductance, G , as a function of E for (a) with various defect concentrations as shown in Fig. S7(c). We can see the calculated conductance of the junction with finite defect concentrations ($P > 0$) is similar to that with $P = 0$. Specifically, the conductance within the gap remain quantized even when P is up to 30%, clearly demonstrating the QSVHK states are robust against the defects, consistent with our analysis based on the symmetry protections. Such a robustness against the defects additionally facilitates the experimental realization and observation of the QSVHK states.

VI. Influence of the Temperature

For applications of topological states, one key point is that the bulk gap, Δ , remains open, which provides a topological protection for the ballistic transport. However, as commonly expected, the temperature-induced thermal excitation can reduce Δ . A common estimate is that the gap remains open when temperature $T < \Delta/k_B$. For room-temperature applications (300 K), the Δ is required to be larger than 26 meV. Since in our proposed BiAs-Bi/SiC junction $\Delta \sim 287$ meV is 10 times larger than 26 meV, it is reasonable to expect that the QSVHK states in BiAs-Bi/SiC junction can be used at room temperature.

In transport calculations, temperature effects can be simulated by using the Fermi-Dirac distribution function, $f = 1/[1 + \exp(\frac{E-E_F}{k_B T})]$, in the conductance calculations, written as [6]

$$G = \frac{2e^2}{h} \int \bar{T}(E) \left(-\frac{\partial f}{\partial E} \right) dE,$$

where $\bar{T}(E)$ is the transmission coefficient. The calculated temperature-dependent conductance is shown in Fig. S8. We can see the energy range supporting quantized conductance decreases as T increases, reflecting the expected temperature influence. However, when $T = 300$ K, there is still a visible range of energy supporting ballistic transport, showing a support for the feasibility of the room-temperature applications.

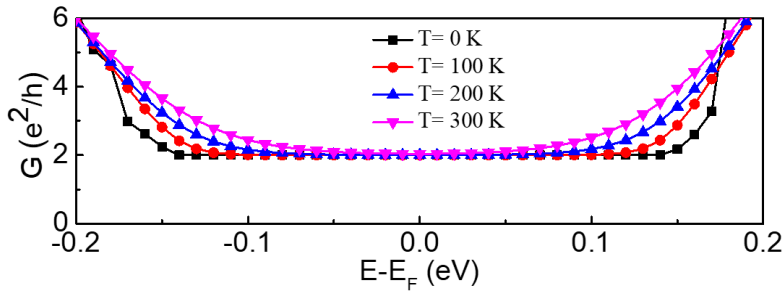


Fig. S8 Temperature-dependent conductance of the QVH-QSH-QVH junction [Fig. S5(a)] as a function of the energy. The parameters are taken from Fig. S5.

The above discussion is based on a single-particle picture, while the electron-electron (e-e) and electron-phonon (e-p) interactions may play important roles at high temperature. Such many-body effects have actually been widely explored in topological states, especially in the QSH system [14]. Since both e-e and e-p interactions induce intervalley scattering [16, 17], the VIS protection for QSVHK states becomes invalid. As a result, the QSVHK degrades into the QSH, which is expected to have a similar behavior as QSH states under electron-electron (e-e) or electron-phonon (e-p) interactions.

For an e-p interaction, since it does not induce spin mixing, the QSH states remain robust when TRS is preserved [17]. For an e-e interaction, it can induce the back scattering in the QSVHK states because both spin and intervalley scattering are allowed even with TRS [14]. However, when the e-e interaction is weak, the QSH states can still remain stable [16, 17]. In typical topological materials (instead of correlated materials), the e-e interactions are usually very weak even at a high temperature [14]. Thus, such many-body interactions have little influence in the QSH states. Besides, the QSH states were detected at 77 K in bismuthene, which is expected to support QSH at room temperature [3]. Since our proposed QSVHK states in BiAs-Bi junction not only share the QSH properties of bismuthene, but also possess an extra protection from the valley-inversion symmetry, it may be reasonable to expect that QSVHK states can survive at room temperature.

VII. Experimental Fabrication

Since the single bismuthene/antimonene/arsenene and their binary films (BiSb and BiAs) have been fabricated [18-19], their planar junctions can be created using our well-established molecular beam epitaxy (MBE) selective area growth and stencil lithography [20]. Specifically, the junction fabrication can be realized in two main steps.

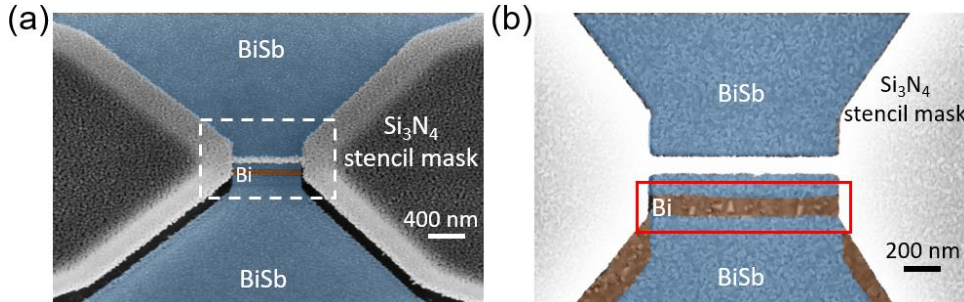


Fig. S9 (a) False color scanning electron micrograph (SEM) image of the planar BiSb-Bi-BiSb junction with a Si₃N₄ stencil mask situated 300 nm above the film for shadowing. (b) The zoom-in of the area marked by the white rectangle in (a), where the BiSb-Bi interfaces are marked by the red rectangle.

I. Fabricating the Si₃N₄ stencil mask for shadowing. Following the process established in our previous work [20], 300 nm of SiO₂ and 100 nm of Si₃N₄ are deposited on a Si (111) substrate via low-pressure chemical vapor deposition (LPCVD). Using electron beam lithography and reactive ion etching, a thin Si₃N₄ stripe as shown in Fig. S9(a) is prepared. Via a following dip into 1% hydrofluoric acid, the SiO₂ under the stripe is etched and the Si₃N₄ bridge is released to create a freestanding bridge. The sample is then transferred into an MBE chamber where it is heated to 700 °C to desorb the hydrogen surface passivation. **II. Spatially-selective growing the BiSb and Bi films.** The Bi and Sb are evaporated respectively from standard Knudsen effusion cells at 530 °C and 475 °C and deposited simultaneously onto the substrate at a growth temperature of 40 °C, similar to the recipe in [21] but without rotating the substrate. The stoichiometry of Bi and Sb can be flexibly controlled by adjusting the fluxes and growth temperature [21]. Since the Bi and Sb molecular beams have high directionality and reach the substrate from different directions, in the shadow cast by the bridge for each beam respectively only the other element is deposited. With the substrate in a well-defined orientation to the stencil bridge with respect to the Sb source, the BiSb film is grown on the substrate, except for the narrow strip [brown in Fig. S9(a)] shaded by the bridge where only pure Bi film is grown. In this way, a planar BiSb-Bi-BiSb junction is created as shown in Fig. S9(b). The desired BiAs-Bi-BiAs junction can also be fabricated using a similar method.

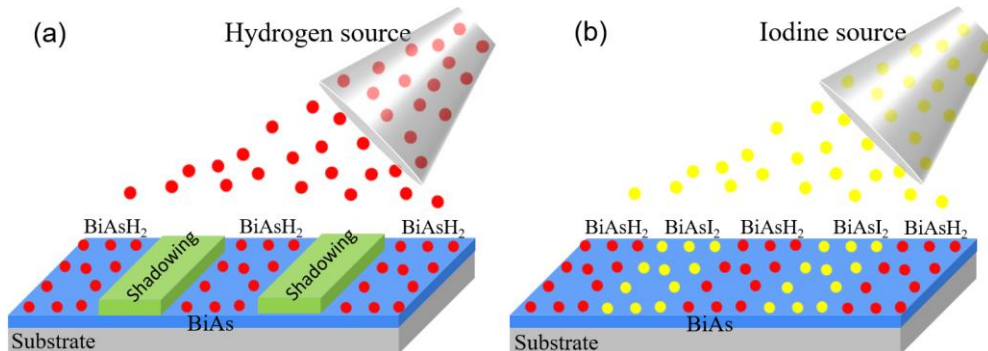


Fig. S10 Schematic of the fabrication of the multiple BiAsH₂-BiAsI₂ junctions with hydrogen and iodine depositions in (a) and (b).

Relying on the similar techniques, we propose a protocol to fabricate multiple BiAsH₂-BiAsI₂ junctions based on the fabricated BiAs film as shown in Fig. S10. First, one can attach several shadow masks on the BiAs film and deposit H atoms. Because of the shadow shields, these H atoms are only deposited on the uncovered regions, bonding with the unsaturated p_z orbitals of the Bi/As atoms and forming BiAsH₂, as shown in Fig. S10(a). Next, one would remove the shadow masks and deposit the iodine atoms. Since the BiAsH₂ regions have been already passivated by the H atoms, the I atoms can only bond with the Bi/As atoms in the non-hydrogenated regions, forming the multiple BiAsH₂/BiAsI₂ junctions as shown in Fig. S10(b). Such techniques have been widely used in chemistry surface functionalization [18, 19].

VIII. Influence of the Stoichiometry

Since the stoichiometry control is crucial for growing binary-element film using MBE, it is important to explore how the stoichiometry affects the electronic and topological properties of the BiAs films. The two key factors in our proposal are the intrinsic SOC, λ_{SO} , and the staggered potential, U, which are both related to the stoichiometry. Thus, it is expected that the stoichiometry plays a significant role.

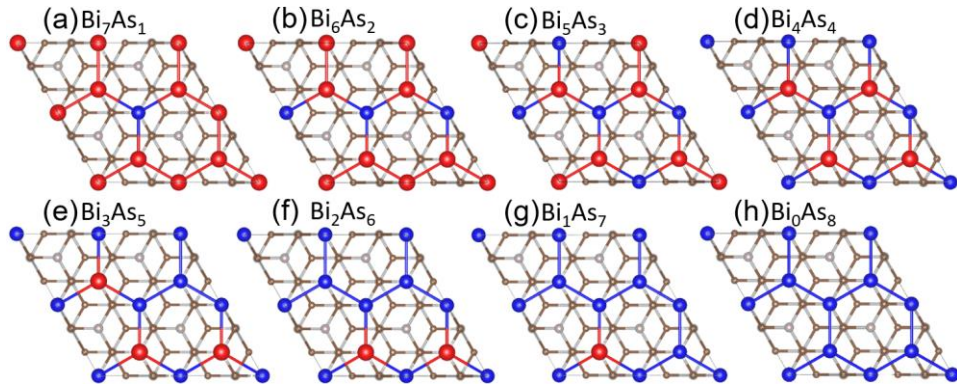


Fig. S11 (a)-(h) Atomic structures of the 2×2 BiAs/SiC supercells with As concentrations from 1/8 to 8/8.

To simulate the influence of the stoichiometry, we created larger 2×2 BiAs/SiC supercells with 1 to 8 As atoms, giving the As-concentration, p_{As} , from 1/8 to 8/8, as shown in Fig. S11. The corresponding electronic structures are shown in Figs. S12(b)-(g). By fitting the effective model with such DFT results, the λ_{SO} and U for different p_{As} are plotted in Fig. S12(a). We can see the λ_{SO} decreases almost linearly with the p_{As} . This is expected since the SOC of As is smaller than that of Bi and the more (less) As (Bi) atoms, the smaller (larger) λ_{SO} is in the BiAs film. For U, Bi₄As₄ gives the maximum U. This can be readily understood since the U indicates the onsite energy difference between the A and B sublattices and the biggest difference emerges when all As (Bi) atoms are at the A (B) sublattice sites, forming the Bi₄As₄ as shown in Fig. S11(d). When some sites of the A (B) sublattice are occupied by the Bi (As) atoms, the U decreases, as in Fig. S12(a). Furthermore, the U vanishes when all sites host the same Bi or As atoms. Such As concentration-dependent competition between U and λ_{SO} determines the gap and topological phase of the BiAs film. Specifically, when $3/8 < p_{As} < 6/8$, $U > \lambda_{SO}$, giving the QVH phase. Otherwise, $U < \lambda_{SO}$, giving the QSH phase as shown in Fig. S12(a). Therefore, to get the QSVHK states, the MBE stoichiometry of As:Bi should be controlled in the range from 3:5 to 6:2. Such a large parameter range gives a considerable flexibility for experimental realization of our proposal. In addition to the MBE growth, the BiAs film can also be fabricated from bulk BiAs crystal using exfoliation [18, 19], which may avoid the concern about the stoichiometry control.

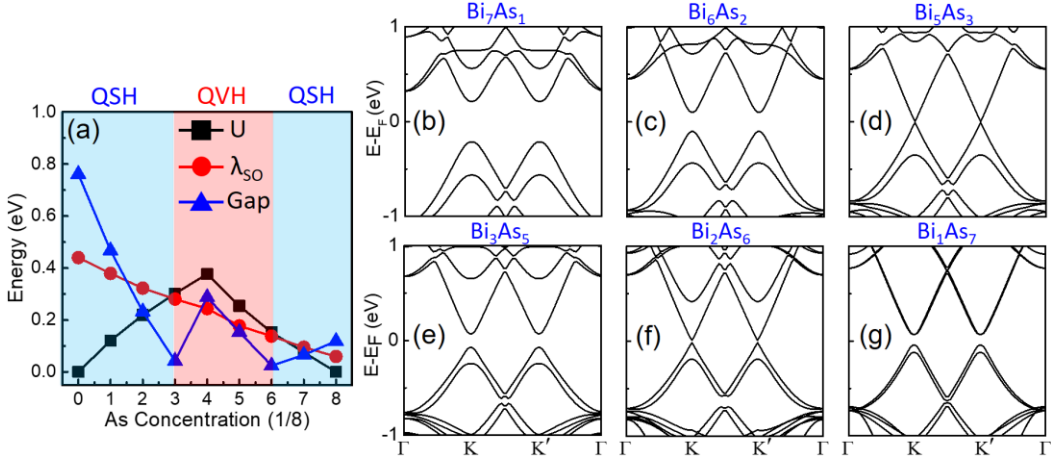


Fig. S12 (a) The As concentration-dependent intrinsic SOC, λ_{SO} , staggered potential, U, and the band gap obtained from the band structures [(b)-(g)] of the corresponding structures in Fig. S11.

The fabricated BiSb-Bi junction and the discussions about the influence of stoichiometry show that our proposed BiAs-Bi junction to realize QSVHK state is promising. The QSVHK states are insensitive to the interface configurations and robust against different nonmagnetic and long-range disorder because of the topological protection. Furthermore, the finite-temperature calculations show the conductance of the QSVHK states remains quantized above room temperature. Taken together, such a strong robustness facilitates the experimental observation of QSVHK states and offers new opportunities in valleytronics and spintronics.

REFERENCES

- [1] G. Kresse, and J. Furthmüller, Efficient iterative schemes for ab initio total-energy calculations using a plane-wave basis set, Phys. Rev. B **54**, 11169 (1996).
- [2] J. P. Perdew, K. Burke, and M. Ernzerhof, Generalized Gradient Approximation Made Simple, Phys. Rev. Lett. **77**, 3865 (1996).
- [3] F. Reis, G. Li, L. Dudy, M. Bauernfeind, S. Glass, W. Hanke, R. Thomale, J. Schafer, and R. Claessen, Bismuthene on a SiC substrate: A candidate for a high-temperature quantum spin Hall material, Science **357**, 287 (2017).
- [4] Y. Yao, L. Kleinman, A. H. MacDonald, J. Sinova, T. Jungwirth, D.-S. Wang, E. Wang, and Q. Niu, First Principles Calculation of Anomalous Hall Conductivity in Ferromagnetic bcc Fe, Phys. Rev. Lett. **92**, 037204 (2004).
- [5] Q. Wu, S. Zhang, H.-F. Song, M. Troyer, and A. A. Soluyanov, WannierTools: An open-source software package for novel topological materials, Comput. Phys. Commun. **224**, 405 (2018).
- [6] S. Datta, Electronic Transport in Mesoscopic Systems (Cambridge University Press, Cambridge, UK, 1997).
- [7] M. P. Lopez-Sancho, J. M. Lopez-Sancho, and J. Rubio, Quick iterative scheme for the calculation of transfer matrices: application to Mo (100), J. Phys. F: Met. Phys. **14**, 1205 (1984).
- [8] T. Zhou, J. Zhang, Y. Xue, B. Zhao, H. Zhang, H. Jiang, and Z. Yang, Quantum spin-quantum anomalous Hall effect with tunable edge states in Sb monolayer-based heterostructures, Phys. Rev. B **94**, 235449 (2016).
- [9] G. Li, W. Hanke, E. M. Hankiewicz, F. Reis, J. Schafer, R. Claessen, C. Wu, and R. Thomale, Theoretical paradigm for the quantum spin Hall effect at high temperatures, Phys. Rev. B **98**, 165146 (2018).
- [10] S. Das Sarma, S. Adam, E. Hwang, and E. Rossi, Electronic transport in two-dimensional graphene, Rev. Mod. Phys. **83**, 407 (2011)

- [11] A. Rycerz, J. Tworzydło, and C. W. J. Beenakker, Anomalously large conductance fluctuations in weakly disordered graphene, *Europhys. Lett.* **79**, 57003 (2007).
- [12] H. Jiang, L. Wang, Q.-F. Sun, and X. C. Xie, Numerical study of the topological Anderson insulator in HgTe/CdTe quantum wells, *Phys. Rev. B* **80**, 165316 (2009).
- [13] Z. Qiao, Y. Han, L. Zhang, K. Wang, X. Deng, H. Jiang, S. A. Yang, J. Wang, and Q. Niu, Anderson Localization from the Berry-Curvature Interchange in Quantum Anomalous Hall Systems, *Phys. Rev. Lett.* **117**, 056802 (2016).
- [14] X.-L. Qi and S.-C. Zhang, Topological insulators and superconductors, *Rev. Mod. Phys.* **83**, 1057 (2011).
- [15] X. Ni, H. Huang, and F. Liu, Robustness of topological insulating phase against vacancy, vacancy cluster, and grain boundary bulk defects, *Phys. Rev. B* **101**, 125114 (2020).
- [16] C. Xu and J. E. Moore, Stability of the quantum spin Hall effect: Effects of interactions, disorder, and Z_2 topology *Phys. Rev. B* **73**, 045322 (2006).
- [17] J. C. Budich, F. Dolcini, P. Recher, and B. Trauzettel, Phonon-induced backscattering in helical edge states, *Phys. Rev. Lett.* **108**, 086602 (2012).
- [18] S. Zhang, S. Guo, Z. Chen, Y. Wang, H. Gao, J. Gómez- Herrero, P. Ares, F. Zamora, Z. Zhu, and H. Zeng, Recent progress in 2D group-VA semiconductors: from theory to experiment, *Chem. Soc. Rev.* **47**, 982 (2018).
- [19] R. Gui, H. Jin, Y. Sun, X. Jiang, and Z. Sun, Two-dimensional group-VA nanomaterials beyond black phosphorus: synthetic methods, properties, functional nanostructures and applications, *J. Mater. Chem. A* **7**, 25712 (2019).
- [20] P. Schügelgen, D. Rosenbach, C. Li, T. W. Schmitt, M. Schleienvoigt, A. R. Jalil, S. Schmitt, J. Kölzer, M. Wang, B. Bennemann, U. Parlak, L. Kibkalo, S. Trelenkamp, T. Grap, D. Meertens, M. Luysberg, G. Mussler, E. Berenschot, N. Tas, A. A. Golubov, A. Brinkman, T. Schäfers, and D. Grützmacher, Selective area growth and stencil lithography for in situ fabricated quantum devices, *Nat. Nanotechnol.* **14**, 825 (2019).
- [21] E. S. Walker, S. Muschinske, C. J. Brennan, S. R. Na, T. Trivedi, S. D. March, Y. Sun, T. Yang, A. Yau, D. Jung, A. F. Briggs, E. M. Krivoy, M. L. Lee, K. M. Liechti, E. T. Yu, D. Akinwande, and S. R. Bank, Composition-dependent structural transition in epitaxial $\text{Bi}_{1-x}\text{Sb}_x$ thin films on Si(111), *Phys. Rev. Mater.* **3**, 064201 (2019).